RESEARCH ARTICLE

NANO · MICRO small
www.small-journal.com

# Single-Phase Solid-Solution Reaction Facilitated Sodium-Ion Storage in Indium-Substituted Monoclinic Sodium-Iron Phosphomolybdate Cathodes

*Sharad Dnyanu Pinjari, Purandas Mudavath, Ravi Chandra Dutta,* Ipsita Pal, Dipan Kundu, Saikumar Parshanaboina, Anand Kumar Singh, Ashok Kumar Nanjundan,* and Rohit Ranganathan Gaddam**

**Despite being a compelling alternative to the existing lithium-ion battery technology, the unavailability of cathodes with high energy density and capacity poses a key challenge toward the wider adaption of sodium-ion batteries (NIB). In this regard, iron-rich NASICONs have triggered significant attention owing to a greater abundance of Fe and higher operating voltages of $Fe^{2+}/Fe^{3+}$ redox-couple. A major roadblock in such cathodes stems from the voltage hysteresis at higher current rates. Herein, a NASICON-type $NaFe_{2-x}In_x(PO_4)(MoO_4)_2$ (NFIPM) cathode is reported that shows a stable single-phase solid-solution reaction with significantly attenuated overpotential. Indium is strategically incorporated at the iron sites, expanding the lattice space to facilitate enhanced sodium-ion diffusion and also reducing the energy bandgap of NFIPM. *Magnetic susceptibility* (M-T) and *Electron Paramagnetic Resonance* (EPR) measurements reveal an increased spin state of iron following indium substitution. *First principle calculations* also confirm the lowering of the $Na^+$ migration energy barrier post indium doping. The optimized NFIPM10 shows a specific capacity of 111.85 mAh $g^{-1}$ at 0.1 C with remarkable cycling stability of up to 800 cycles at 2C. In situ X-ray diffraction confirms reversible structural stability of NFIPM during (de)sodiation, emphasizing the role of strategic doping in enhancing sodium-ion storage.**

## 1. Introduction

Sodium-ion batteries (NIBs) are sought after as a resource-saving, sustainable alternative energy storage technology to lithium-ion batteries.[1] Despite the chemical similarity between sodium and lithium, a severe energy density deficit makes NIBs less attractive for industrial adoption. The unavailability of low-cost cathodes with better sodium-ion uptake at high working voltages and superior cycling stability poses a critical challenge. Polyanion or mixed-polyanionic type cathodes, with their unique 3D structural make-up, have gained significant interest in addressing these limitations. These cathodes explore redox-chemistries of earth-abundant materials that can expedite the market readiness of NIBs.[2]

Notably, considerable research has been devoted to sodium super ionic conductor (NASICON)-type polyanions that exist either in a rhombohedral (R-3c) or monoclinic (C2/c) symmetry.[3] Such

S. D. Pinjari, P. Mudavath, S. Parshanaboina, A. K. Singh, R. R. Gaddam
Department of Chemical Engineering
Indian Institute of Science Education and Research-Bhopal
Bhopal, Madhya Pradesh 462066, India
E-mail: rohitg@iiserb.ac.in

R. C. Dutta
Department of Chemical Engineering
Indian Institute of Technology Dharwad
Dharwad, Karnataka 580011, India
E-mail: ravicd@iitdh.ac.in

The ORCID identification number(s) for the author(s) of this article can be found under https://doi.org/10.1002/smll.202501004



DOI: 10.1002/smll.202501004

R. C. Dutta
School of Chemical Engineering
The University of Queensland
Brisbane, QLD 4072, Australia

I. Pal, D. Kundu
Department of Chemical Engineering
UNSW, UNSW
Sydney, NSW 2052, Australia

A. K. Singh
Material Science and Engineering
National University of Singapore (NUS)
Singapore 117575, Singapore

A. K. Nanjundan
Australia Centre for Future Materials and the School of Engineering
University of Southern Queensland
Brisbane, QLD 00244B, Australia
E-mail: ashok.nanjundan@unisq.edu.au

compounds have a general formula of $Na_xMM'(XO_4)_3$ where M and M' are multivalent cations and $XO_4$ represents the polyanion. Here, the metal octahedra and the polyanion tetrahedra share corners forming 3D channels that facilitate faster sodium-ion transport and provide better structural integrity. A major roadblock in the NASICON cathode stems from its higher energy band gap and sodium-ion storage at relatively lower voltages.[4]

In order to increase the mean voltage and energy density of the cathode, the inductive effect of highly electronegative polyanion groups is leveraged by introducing them into the NASICON backbone.[5] In this regard, Goodenough et al. first reported the high-voltage iron phospho-sulfate cathode $NaFe_2(PO_4)(SO_4)_2$ using a low-temperature synthesis method.[6] Their electrochemical analysis indicates a single-phase reaction for $Na_{1+x}Fe_2(PO_4)(SO_4)_2$ (where $0 \leq x \leq 2$) with an average working voltage of 3.15 V versus $Na/Na^+$. However, this material exhibited unusual cycling behavior due to unoptimized morphology and reduced phase purity. Building on the initial work, several attempts have been made to synthesize high-quality $NaFe_2(PO_4)(SO_4)_2$ by employing different experimental approaches such as sol-gel, solid-state, and chemo-mechanical synthesis.[5b,7] In another work, Kim et al. reported a Fe-centered NASICON-type cathode, $Na_4Fe_3(PO_4)_2(P_2O_7)$, by including two polyanionic groups, $(PO_4)^{3-}$ and $(P_2O_7)^{4-}$.[8] This cathode demonstrates a remarkable discharge-specific capacity, 88% of its theoretical capacity (129 mAh $g^{-1}$) at a slow current rate of C/40, with an average redox potential of 3.2 V versus $Na/Na^+$. Zhang et al. further optimized this structure by doping $(SiO_4)^{4-}$ in place of $(PO_4)^{3-}$ resulting in $Na_4Fe_3(PO_4)_{1.9}(SiO_4)_{0.1}(P_2O_7)$, which demonstrates an improved $Na^+$ uptake from 103.2 to 108.7 mAh $g^{-1}$ at 0.1C.[9] Additionally, pairing the sulfate $(SO_4)^{2-}$ polyanion with phosphate $(PO_4)^{3-}$ can significantly enhance cathode performance due to the high electronegativity of sulfate.[5b,7] On the other hand, phosphomolybdate-based NAISCON cathodes, $NaFe_2(PO_4)(MoO_4)_2$ (NFPM), exhibit distinct characteristics by making use of transition metal in its polyanion group.[1d] For example, the larger size of the $(MoO_4)^{2-}$ enhances Na ion mobility by offering wider diffusion channels, while the 3d orbital of Mo helps attenuate the bandgap. The initial electrochemical investigation of Gao et al. demonstrated that this cathode shows a sloping voltage profile with a $Na^+$ storage capacity of 86 mAh $g^{-1}$ at 0.1 C.[1d] However, significant voltage hysteresis, low cycling stability, and marginal specific capacity of NFPM highlight the critical need for further optimization and development of such cathode material.

Here, for the first time, we report $NaFe_{2-x}In_x(PO_4)(MoO_4)_2$, through a straightforward solid-state reaction, with $In^{3+}$ substituted at Fe-site. Indium is chosen as a dopant due to its unique chemical and structural properties. Theoretically, its low ionization energy and electronic configuration enable it to function as an effective donor or acceptor, making it ideal for tuning the electrical conductivity, thermal stability, and ionic conductivity of materials.[10] Moreover, indium's atomic radius and chemical compatibility allow it to integrate into crystal lattices with minimal structural changes, ensuring long-term stability. Despite this, indium has not been explored as a dopant in phosphomolybdate-based NASICON-type cathodes. Our experimental findings and first-principles calculations reveal that partial substitution of $In^{3+}$ for $Fe^{3+}$ stabilizes the crystal structure, enhances $Na^+$ diffusion kinetics, improves electrical conductivity, and reduces the energy bandgap and cell polarization. Interestingly, the optimal structure, $NaFe_{1.9}In_{0.1}(PO_4)(MoO_4)_2$ (referred to as NFIPM10), achieves a maximum specific discharge capacity of 111.85 mAh $g^{-1}$ at 0.1C, with an impressive energy density of 280 Wh $kg^{-1}$. Furthermore, NFIPM10 demonstrates ≈82% capacity retention over the first 100 cycles and 75% over 650 cycles (based on 100 cycles as an initial capacity) at 0.1 C. At a current rate of 0.2 C, it maintains ≈80% capacity retention over 200 cycles, and at a high current rate of 2C, it shows remarkable cycling stability over 800 cycles. The enhanced performance of the NFIPM cathode through $In^{3+}$-doping is thoroughly analyzed using GITT, in situ EIS, DRT (distribution relaxation time), in situ XRD, XPS, and electrical conductivity measurements. Additionally, Density Functional Theory (DFT) calculations complement the experimental observations of enhanced lattice parameters and lowered energy bandgap post-doping. We believe our findings will offer valuable insights into NFIPM cathodes and their potential for practical applications in NIBs.

## 2. Results and Discussion

### 2.1. Structure and Morphology

The thermogravimetric (TG) analysis shows that NFIPM is thermally stable up to 750 °C with a carbon content of 6.20, 1.06, 1.53, 5.54, 3.02, and 2.57 wt.% for x = 0.0, 0.05, 0.07, 0.10, 0.20 and 0.30 respectively (**Figure 1a**). This suggests that $In^{3+}$ incorporation significantly influences the thermal stability of the NFIPM samples. Notably, all doped compositions exhibit lower decomposition compared to the undoped sample (NFIPM00), indicating that doping enhances the structural stability of the material. Furthermore, NFIPM00, NFIPM10, and NFIPM30 exhibit early weight loss during TG analysis, which is likely attributed to the presence of residual solvents from the precursor solution, leading to evaporation at lower temperatures. Based on the TG analysis results, the temperature for the synthesis of NFIPM was fixed at 600 °C. The NASICON structures for the NFIPM samples were confirmed via powder X-ray diffraction (PXRD) patterns (Figure 1b), where all peaks can be indexed to a monoclinic phase (space group: P2/c). The sharper diffraction peaks post-doping indicate an improved crystallinity in NFIPM samples. As the content of $In^{3+}$ was increased, the XRD peaks corresponding to the plane of (112) and (420) shifted leftward (zoomed-in spectra of Figure 1b) indicating successful substitution of dopant at the Fe-site. Detailed crystallographic parameters for NFIPM cathodes were evaluated using Rietveld refinement via the Fullprof software (Figure 1c,d; S1, Supporting Information). The lattice parameters show an increase in cell volume postdoping (Figure S2a, Supporting Information) due to the larger ionic radius of $In^{3+}$ (r = 0.81 Å) than $Fe^{3+}$ (0.64 Å).[11] The cell parameters *a*, *b*, and *c* also increased with $In^{3+}$-substitution, it follows no particular trend related to the doping content, probably due to the random distribution of $In^{3+}$ into the $Fe^{3+}$ site. Further, compared with NFIPM00 data ($a$ = 12.76 Å, $b$ = 8.99 Å, $c$ = 9.17 Å, and $v$ = 1052.95 $Å^3$), the cell parameters ($a$ = 12.81 Å, $b$ = 9.00 Å, $c$ = 9.18 Å, and $v$ = 1058.31 $Å^3$) of NFIPM10 show that the substitution of $In^{3+}$ enlarges the lattice sites leading to a

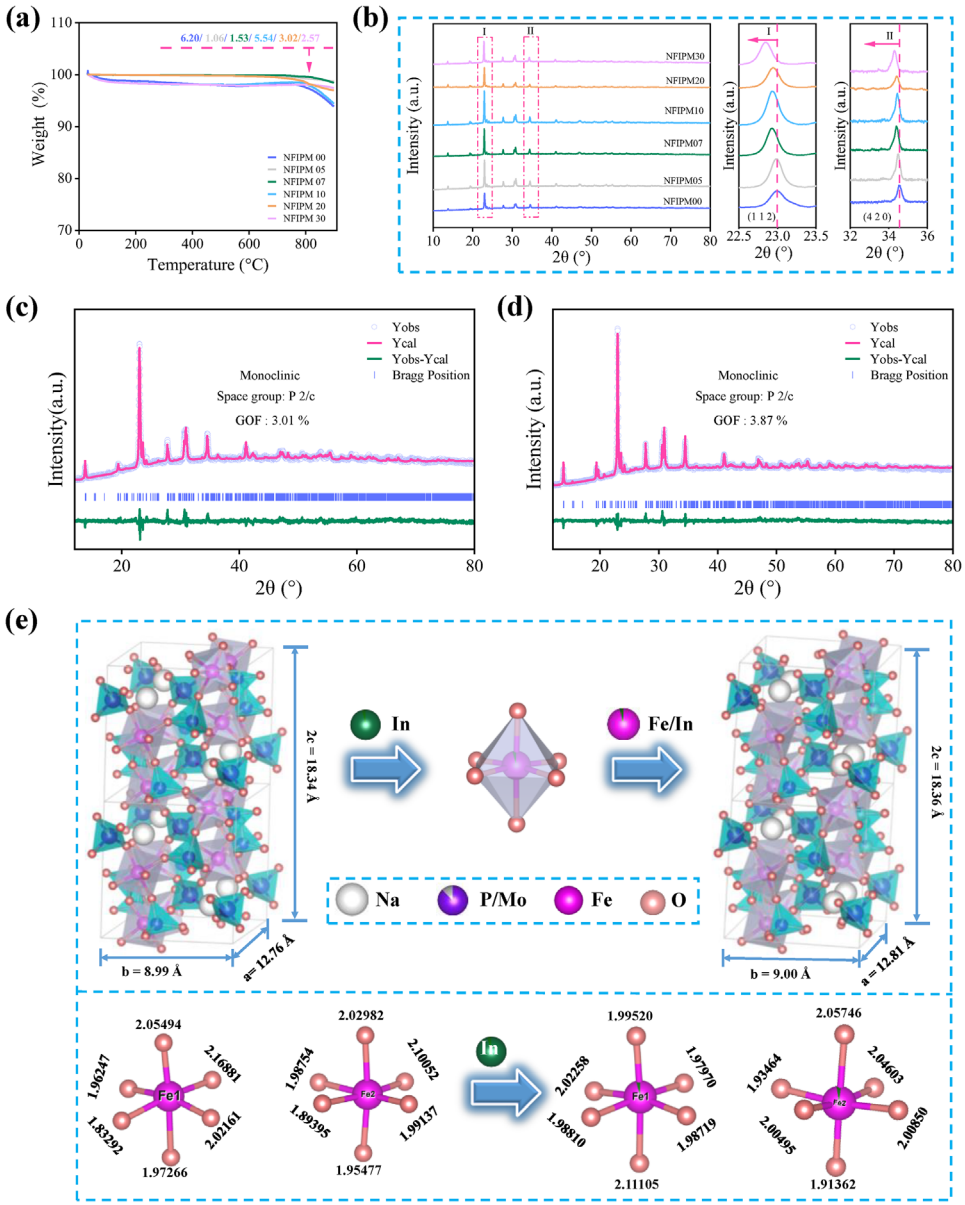


**Figure 1.** a,b) TG profiles and XRD patterns show peak shifts corresponding to the (112) and (420) planes for all NFIPM samples. c,d) Represents the XRD Rietveld refinement results for NFIPM00 and NFIPM10, respectively. e) Structural schematic and the changes in Fe—O bond lengths due to indium substitution in NFIPM00.

slight distortion in structure. The average bond length of Fe—O (1.9975 Å) and Na—O (2.53096 Å) of NFIPM00 is shorter than NFIPM10 (Fe—O = 2.0041 Å, and Na—O = 2.54423 Å). A longer Na—O bond length provides a larger interstitial space, reduces the energy barrier, and enhances $Na^+$ diffusion kinetics. The detailed crystal data including atomic positions, site occupancy, and isothermal parameters for each composition are given in Tables S1–S6 (Supporting Information). According to the Wyckoff positions, there are 19 atoms positioned in their respective crystallographic sites. Among them, Mo/P forms one tetrahedron ($Mo/PO_4$) coordinated with four oxygen atoms and Fe/In forms a single octahedron ($Fe/InO_6$) coordinated with six oxygen atoms. A robust 3D framework of NFIPM cathode is formed via the linkage of these octahedrons and tetrahedrons units through oxygen-sharing (Figure 1e). The FTIR analysis of the samples reveals characteristic infrared absorption peaks related to Fe—O bonds in the octahedra and Mo/P—O bonds in the tetrahedra of the NFIPM structure (**Figure** 2a; S2b, Supporting Information). In particular, the peaks ≈1134 and 974 $cm^{-1}$ correspond to the bending (O—P—O) and stretching (P—O) vibrations of the $PO_4$ polyanion, while peaks ≈630 and 550 $cm^{-1}$ are associated with Fe—O stretching vibrations.[12] A broad peak ≈789 $cm^{-1}$ indicates the presence of molybdate ($MoO_4$) in NFIPM.[13] Raman spectra for NFIPM00 and NFIPM10 (Figure 2b) display two peaks at ≈252 and 352 $cm^{-1}$, reflecting the symmetric and antisymmetric bending modes ($\nu_2$ and $\nu_4$) of the $MoO_4^{2-}$ anion.

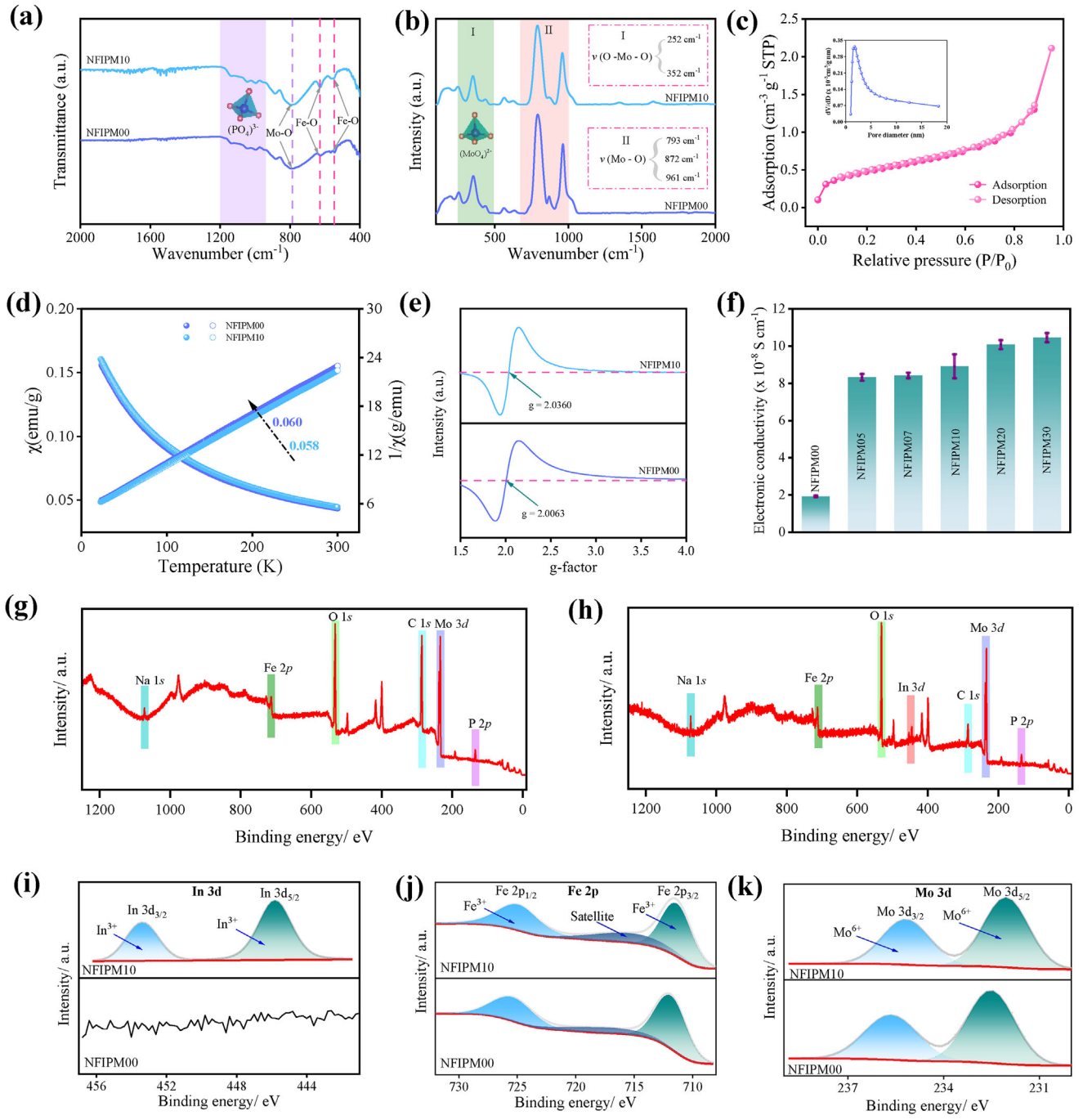


**Figure 2.** Characterization of NFIPM cathodes. a,b) Represents the FTIR patterns and Raman scattering spectra for NFIPM00 and NFIPM10 respectively. c) The nitrogen adsorption-desorption isotherms along with the pore size distribution (inset) for NFIPM10. d) Temperature-dependant magnetic susceptibility profiles for NFIPM00 and NFIPM10. e,f) EPR spectrum and electrical conductivity measurements for all NFIPM materials. g,h) The scan XPS survey and i–k) Deconvoluted spectrum of In 3d, Fe 2p, Mo 3d in NFIPM00 and NFIPM10 respectively.

Additional peaks at ≈793, ≈872, and ≈961 $cm^{-1}$ correspond to the symmetric and antisymmetric vibrations ($\nu_1$ and $\nu_3$) of the $MoO_4$ tetrahedron.[14] The specific surface area and pore size distribution of the NFIPM10 samples were analyzed using the $N_2$ sorption experiment (Figure 2c). NFIPM10 exhibits a higher Brunauer–Emmett–Teller (BET) surface area and smaller pore size (1.7388 $m^2$ $g^{-1}$, 4.02 nm) compared to NFIPM00 (Figure S2c, Supporting Information) sample (1.6909 $m^2$ $g^{-1}$, 4.21 nm). The enhanced specific surface area and smaller pore size distribution enhance electrolyte percolation allowing for the full capacity of the electrode to be realized.[15] Temperature-dependent magnetic susceptibility ($\chi$ = M/H) measurements were conducted

 

to quantify the magnetic properties of NFIPM00 and NFIPM10 (Figure 2d). The samples exhibited Curie–Weiss paramagnetic behavior within the temperature range of 50 to 300 K. The plot of $1/\chi$ versus T displayed a linear trend with a lower slope for NFIPM10 compared to the NFIPM00. These results indicate that doping enhances the paramagnetic properties of the material, along with an increase in the Pauli paramagnetism of free electron spins within the iron centers.[16] Electron paramagnetic resonance (EPR) measurements were also conducted to investigate the energy levels of free electrons in both samples. This analysis typically reveals the g-factor and offers insights into the spin states of free electrons under an applied magnetic field. The EPR profiles show a slight shift to the right following $In^{3+}$ incorporation (Figure 2e). Variations in g-values arise from changes in the angular momentum of free electrons. Notably, the increased g-values post $In^{3+}$ substitution suggest an enhanced spin state of Fe in the NFIPM10 sample.[17] To further validate these findings, the electrical properties of NFIPM materials were evaluated using two-point probe conductivity measurements. The average electrical conductivity values for NFIPM00, NFIPM05, NFIPM07, NFIPM10, NFIPM20, and NFIPM30 are $1.92 \times 10^{-8}$, $8.32 \times 10^{-8}$, $8.42 \times 10^{-8}$, $8.91 \times 10^{-8}$, $10.07 \times 10^{-8}$, and $10.50 \times 10^{-8}$ S $cm^{-1}$, respectively (Figure 2f). These results show that indium doping boosts the electrical conductivity of NFIPM cathodes. The X-ray photoelectron spectroscopy (XPS) measurements were used to detect the valance state of elements present in the NFIPM00 and NFIPM10 samples. While XPS is a surface analysis technique, to ensure that the obtained results reflect the composition of the bulk, the material was thoroughly ground and then pressed into a pellet to ensure uniform mixing. The recorded survey spectra of both samples show the peaks of Na 1s, O 1s, C 1s, Fe 2p, In 3d, P 2p, and Mo 3d (Figure 2g,h). The deconvoluted spectra of each element are shown in Figure 2i–k and S3 (Supporting Information). The intense peaks positioned at 712 eV (Fe $2p_{3/2}$), and 725 eV (Fe $2p_{3/2}$) are the characteristic peaks of $Fe^{3+}$ (Figure 2j).[1d,18] Therefore, it is confirmed that $Fe^{3+}$ is not reduced during the high-temperature treatment. The additional signal observed ≈716 eV can be attributed to the satellite peak.[19] Further, the Mo 3d high-resolution spectra (Figure 2k) were deconvoluted into two peaks at 232.05 and 235.25 eV corresponding to Mo $3d_{5/2}$ and Mo $3d_{3/2}$ respectively [20]. Similarly, the In 3d spectra (Figure 2i) reveal two weak peaks deconvoluted at 445.81 eV (In $3d_{5/2}$) and 453.41 eV (In $3d_{3/2}$), confirming the presence of $In^{3+}$ in the NFIPM10 sample [21]. Scanning electron microscope (SEM) images of NFIPM00 and NFIPM10 clearly show that samples are almost cubic (Figures S4a,b, and S5a–c, Supporting Information) and doping has little effect on the surface morphology. High-resolution transmission electron microscope (HR-TEM) images reveal that both NFIPM00 and NFIPM10 are crystalline in nature (**Figure 3**a,b; S6a, Supporting Information). A carbon layer of thickness 3–4 and 1.5–2.5 nm was also observable in NFIPM00 and NFIPM10 samples respectively (Figure 3c; S6, Supporting Information). This layer is likely formed due to the pyrolysis of citric acid during the in-situ sintering process.[22] The selected area electron diffraction (SAED) patterns indexed to the plane of (31-1), (412), and (612) for NFIPM00 (Figure S6c) and (424), (41-6), and (436) for NFIPM10 (Figure 3d) exhibits a sharp spot which indicates a long-range order structure. The interplanar spacing corresponding to FFT analysis for all NFIPM samples was evaluated from the TEM images (Figure 3e,f; S6d,e and Figure S10, Supporting Information). The d-spacing for NFIPM00, NFIPM05, NFIPM07, NFIPM10, NFIPM20, and NFIPM30 samples are 0.3867 nm (12-1), 0.4125 nm (012), 0.4232 nm (020), 0.4397 nm (10-2), 0.5060 (210), and 0.6783 nm (011) respectively. This confirms that $In^{3+}$-doping increases the lattice spacing of NFIPM, which aligns well with the results from Rietveld refinement of XRD profiles. The enlarged interlayer spacing post-doping contributes to the improved electrochemical performance of NFIPM cathodes by facilitating $Na^+$ kinetics during the cycling process. Further, the SEM energy dispersive X-ray (EDX) elemental mapping of NFIPM00 (Figure S4c–i, Supporting Information), NFIPM10 (Figure S5d–k, Supporting Information), and TEM-EDX elemental mapping of all NFIPM samples (Figure 3g–n; S6f–o, S7–S9, Supporting Information) illustrate an even distribution of Na, Fe, P, Mo, C, O, and In dopant throughout the material.

### 2.2. Electrochemical Measurements

The electrochemical properties of all NFIPM cathodes were tested against sodium in a half-cell configuration. **Figure** 4a illustrates the galvanostatic charge/discharge performance of each composition within the voltage range of 1.5–3.8 V versus $Na/Na^+$ and at a current rate of 0.1C. The specific discharge capacities for NFIPM00, NFIPM05, NFIPM07, NFIPM10, NFIPM20, and NFIPM30 are 97.36, 100.04, 105.96, 111.85, 102.04, and 86.81 mAh $g^{-1}$, respectively. Notably, the initial discharge capacities of the $In^{3+}$-doped samples are higher than those of the undoped sample, except for NFIPM30. Additionally, the $Na^+$ storage capacity improves as the amount of $In^{3+}$ in the sample increases. This can be due to the higher size of $In^{3+}$ which facilitates charge transfer rate by expanding the lattice framework. Amongst all samples, NFIPM10 performs best and delivers the first cycle charge/discharge capacity of 107.47/111.85 mAh $g^{-1}$ (at 0.1C) with a Coulombic efficiency of 96%. It is observed that the substituting $In^{3+}$ beyond x = 0.10 is detrimental to the electrode performance as it reduces the electro-active Fe content in the sample. Moreover, the charge/discharge profiles of NFIPM00 and optimized NFIPM10 at various C- rates are shown in Figure 4b,c respectively. Even at a high current rate of 1C, NFIPM10 delivers a remarkable discharge capacity of 80.58 mAh $g^{-1}$. The rate performance of all NFIPM electrodes was evaluated at different current rates ranging from 0.1 to 10C (Figure 4d). NFIPM00 exhibits specific discharge capacities of 97.53, 88.18, 72.93, 61.63, 56.95, 23.14, and 3.55 mAh $g^{-1}$ at current rates of 0.1, 0.2, 0.5, 1, 2, 5, and 10C, respectively. NFIPM10 demonstrates discharge capacities of 111.59, 101.59, 89.65, 80.58, 65.67, 42.64, and 22.65 mAh $g^{-1}$ at the same rates. The optimized cathode consistently showed significant improvements in discharge capacities across all current rates. Particularly, NFIPM10 exhibited less capacity fading compared to NFIPM00. After 48 cycles and enduring a significant charge-discharge current rate of 10C, NFIPM00 retained 95.52% of its capacity at 0.1C, while NFIPM10 achieved a retention of 98%. At the high current rate of 10C, NFIPM00 displayed a minimal capacity retention of only 3.63% of its initial

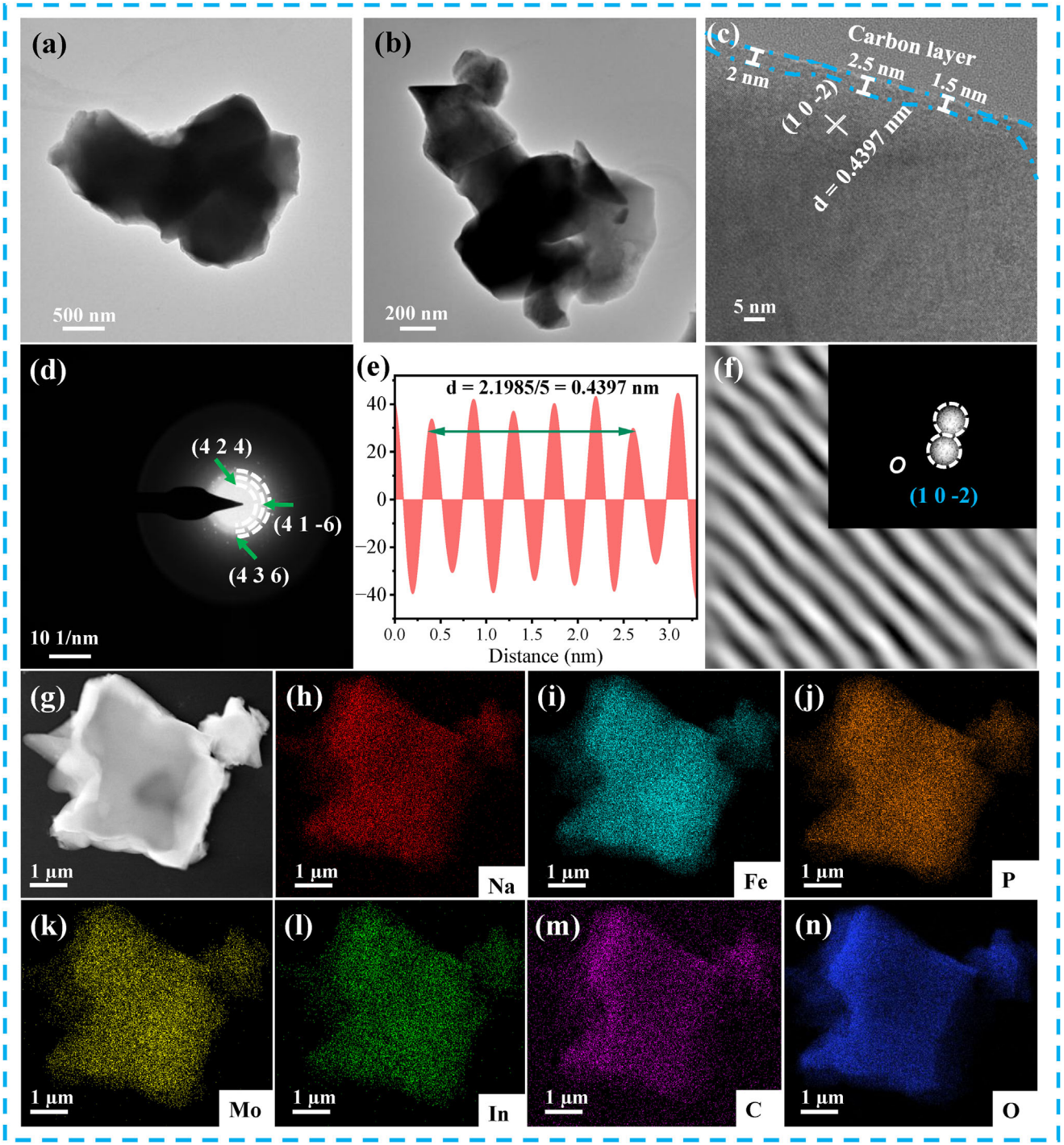


**Figure 3.** a,b) HRTEM image, c) Lattice fringes, d) SAED patterns, e) d-spacing and f) Corresponding FFT, g) HAADF image and h–n) elemental mapping of NFIPM10 sample.

capacity, whereas NFIPM10 fared better with a capacity retention of 20.4%.

These results indicate that the optimization of dopant plays a significant role in the enhancement of the $Na^+$ storage capacities of NFIPM cathodes. In addition to charge storage capacity and rate capability, evaluating the cycling performance of NFIPM cathodes at various current rates is crucial for large-scale energy storage devices. In this regard, cycling stability tests were carried out at current rates of 0.1, 0.2, 1, and 2C. At 0.1C, for over 100 cycles, the discharge capacities for NFIPM00, NFIPM05, NFIPM07, NFIPM10, NFIPM20, and NFIPM30 were 80.70, 87.31, 88.59, 91.57, 86.52, and 75.91 mAh $g^{-1}$, respectively

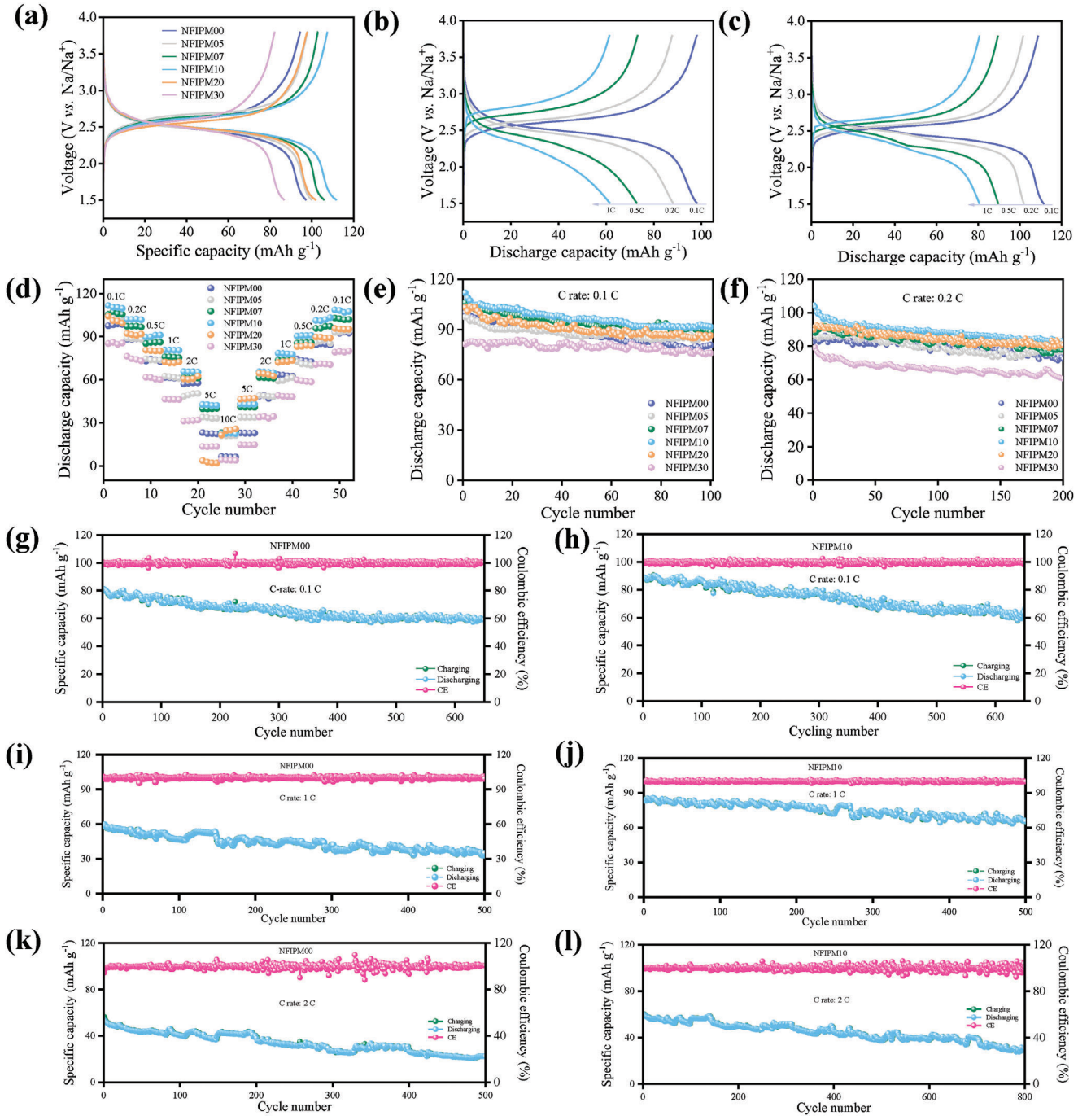


**Figure 4.** Electrochemical performance of prepared NFIPM cathodes in the voltage range of 1.5–3.8 V. a) The initial charge–discharge curves obtained at a current rate of 0.1 C. b,c) Charge–discharge profiles at different current rates of 0.1, 0.2, 0.5, and 1 C of NFIPM00 and NFIPM10 respectively. Rate capability test d), cycling performance e) at 0.1C, and f) at 0.2 C for all electrodes. Long-term cycling of g) NFIPM00, h) NFIPM10 at 0.1C plotted after completing initial 100 cycles. Similarly, cycling stability was evaluated at high current rate of 1C for i) NFIPM00, j) NFIPM10 and at 2C for k) NFIPM00 and l) NFIPM10.

(Figure 4e; Figure S11, Supporting Information). All indium-doped samples showed better capacity retention than the un-doped sample.

NFIPM10 achieved ≈82% retention compared to 80% for NFIPM00 over 100 cycles. Especially, after 650 cycles, NFIPM00 retained 71% capacity (Figure 4g) while NFIPM10 had a 75% retention (Figure 4h) (both capacity retention calculated based on their initial discharge capacities over 100 cycles). We deliberately conducted this long-term cycling stability test at a low current rate of 0.1C to assess the material's durability over an extended period. The results showed that NFIPM00 and NFIPM10 exhibited excellent stability over 369 days. Further, at a current rate

of 0.2 C, NFIPM10 delivers a discharge capacity of 83 mAh $g^{-1}$ over 200 cycles, the highest among all samples (Figure 4f). Also, over 500 cycles at 1C, NFIPM00 show ≈59% retention while NFIPM10 exhibits a remarkable retention of ≈80% (Figure 4i,j). Additionally, at a high current rate of 2C, NFIPM00 showed a capacity of 56.30 mAh $g^{-1}$ with 39% retention after 500 cycles (Figure 4k). In contrast, NFIPM10 demonstrated an impressive discharge capacity of 63.47 mAh $g^{-1}$, maintaining ≈64% capacity retention after 500 cycles and ≈50% over 800 cycles (Figure 4l). Figure 4 shows that NFIPM00 and NFIPM10 exhibit minimal performance differences at low current rates (at 0.1, 0.2C) compared to high current rates (at 1, 2C). At low currents, $Na^+$ has sufficient time to shuttle between the anode and cathode, resulting in greater cell polarization. However, at higher current rates, the faster movement of $Na^+$ reduces resistive losses, minimizing the impact of cell polarization.[23] Also, the overall Coulombic efficiency approached ≈100% highlighting the high reversible $Na^+$ storage behavior of cathodes. Overall, optimal $In^{3+}$ doping plays a crucial role in enhancing charge/discharge capacities, rate performance, and cycling stability of the cathode materials. The cyclic voltammograms (CV) for all NFIPM cathodes, recorded at a scan rate of 0.10 mV $s^{-1}$, are presented in Figure S12 (Supporting Information). Within the voltage range of 1.5–3.8 V versus $Na/Na^+$, all samples exhibit a distinct redox peak, which can be attributed to the $Fe^{2+}/Fe^{3+}$ couple. The redox peaks for NFIPM00, NFIPM05, NFIPM07, NFIPM10, NFIPM20, and NFIPM30 are located at 2.91/2.32, 2.81/2.39, 2.85/2.35, 2.86/2.40, 2.69/2.39, and 2.67/2.38 V, respectively, with corresponding peak separations ($\Delta V = V_{anodic} - V_{cathodic}$) of 0.59, 0.42, 0.50, 0.46, 0.30, and 0.29 V. The degree of separation between the anodic and cathodic peaks reflects the cell polarisation along with the overall reversibility of the electrochemical reaction.[24] Notably, all indium-doped samples exhibit a smaller peak separation than undoped samples. This result indicates that doping significantly reduces cell polarisation and enhances the $Na^+$ kinetics. A similar observation was made in charge-discharge profiles obtained at 0.1C current rate (Figure S13, Supporting Information). CVs of NFIPM10 at various scan rates of 0.10, 0.15, 0.20, 0.25, and 0.30 mV $s^{-1}$ are shown in **Figure** 5a. Similar profiles for NFIPM00, NFIPM05, NFIPM07, NFIPM20, and NFIPM30 can be found in Figure S14 (Supporting Information). It can be observed that, as the scan rates increase from 0.1 to 0.30 mV $s^{-1}$, all curves retain their overall shape, with only minor shifts in the redox peaks. Particularly, NFIPM00 exhibits the polarisation voltage (ΔV) of 0.58 and 0.95 V at a sweep rate of 0.10 and 0.30 mV $s^{-1}$ respectively. In contrast, NFIPM10 shows values of 0.46 and 0.64 V at the same sweep rates. Thus, even at a higher sweep rate, NFIPM10 offers lower polarization. Additionally, the reversibility of the electrochemical reaction was examined by conducting repeated CV tests (5 cycles) at the same scan rate ($\nu$ = 0.15 mV $s^{-1}$). The profiles for all NFIPM cathodes displayed overlapping curves (Figure S15, Supporting Information), indicating a highly reversible $Na^+$ reaction. For the first time, sharp CV and flat charge/discharge profiles for iron phosphomolybdate cathodes are demonstrated here through our work. This observation indicates the occurrence of a single-phase solid-solution reaction during the $Na^+$ insertion/deinsertion process (also confirmed via in-situ XRD analysis). $Na^+$ transport kinetics was further evaluated using a detailed analysis of CVs at different scan rates. The linear relationship between peak currents ($i_{pa}$, $i_{pc}$) versus square root of scan rates ($\nu^{1/2}$) was observed in all NFIPM cathodes (Figure 5b). Therefore, the $Na^+$ diffusion co-efficient ($D_{Na+}$) was determined using the following Randle—Sevcik equation:[25]

$$I_p = \left(2.69 \times 10^5\right)\ n^{3/2}\ A\ \left(D_{Na^+}^{1/2}\right)\ \left(C_{Na^+}\right)\left(\upsilon^{\frac{1}{2}}\right) \quad (1)$$

where n is the electrons transfer per mole in reaction, A is the electrode area (0.785 $cm^2$), $C_{Na+}$ is the bulk concentration of $Na^+$ within the electrode (in mol $cm^{-3}$), and $\nu$ indicates the scan speed (V $s^{-1}$). The obtained slope and apparent $Na^+$ diffusion coefficients for NFIPM cathodes are shown in Tables S7 and S8 (Supporting Information) respectively. Specifically, NFIPM10 has a $D_{Na+}$ values of $1.74 \times 10^{-9}$ and $1.29 \times 10^{-9}$ $cm^2$ $s^{-1}$ for desodiation and sodiation respectively (Figure S17b, Supporting Information). In contrast, NFIPM00 shows $D_{Na+}$ values of $2.14 \times 10^{-11}$ and $0.91 \times 10^{-11}$ $cm^2$ $s^{-1}$ for desodiation and sodiation respectively. The higher $D_{Na+}$ values for NFIPM10 compared to NFIPM00 can be attributed to $In^{3+}$-substitution, which increases the interlayer spacing, shortens the diffusion pathways, and enhances the $Na^+$ transport. The reaction kinetics and type of $Na^+$ insertion and extraction in all cathodes were depicted using the following relations,[26]

$$i_p = a\nu^b \quad (2)$$

$$\log\left(i_p\right) = b\log\left(\nu\right) + \log\left(a\right) \quad (3)$$

$$ip = k_1\nu + k_2\nu^{1/2} \quad (4)$$

where a, b, $k_1$, $k_2$ are the constant parameters can be determined using the values of peak currents recorded at various sweep rates. Typically, the explored battery materials exhibit charge storage properties that are a blend of capacitive and Faradaic behavior. The slope of the plot log ($i_p$) versus log ($\nu$) discloses the b values. When the b value is ≈0.5 indicates the Faradic process controls the reaction while ≈1.0 indicates the surface-controlled pseudocapacitive behavior. The obtained values of b for all cathodes are shown in Figures S16 and S17a (Supporting Information). Furthermore, the percentage contribution of each process was determined using Equation (4). The intercept and slope of the plot of $i_p/\nu^{1/2}$ versus $\nu^{-1/2}$ were used to evaluate $k_1$ and $k_2$ values. The results of capacitive contribution and diffusion contribution are shown in Figure 5c,d, and Figure S16 (Supporting Information). The kinetic analysis shows that both mechanisms play a vital role in $Na^+$ storage to enhance the overall performance of cathodes. To further understand the phase transition, electrode kinetics, and reversible $Na^+$ storage in all samples, the differential capacity (dQ/dV vs V) profiles of the first 100 cycles (starting from 2nd cycle) were recorded at a constant current rate of 0.1C (Figure 5e,f; Figure S17c–f, Supporting Information). The area beneath the curve reflects the charge storage capacity. Additionally, the plateau in the charge-discharge profiles (voltage vs capacity) manifests as a peak in the differential capacity plot. A flat plateau in these profiles corresponds to a sharp peak in the dQ/dV vs V plot. In differential capacity plots, like the CV profiles, each cathode shows a distinct peak corresponding to the

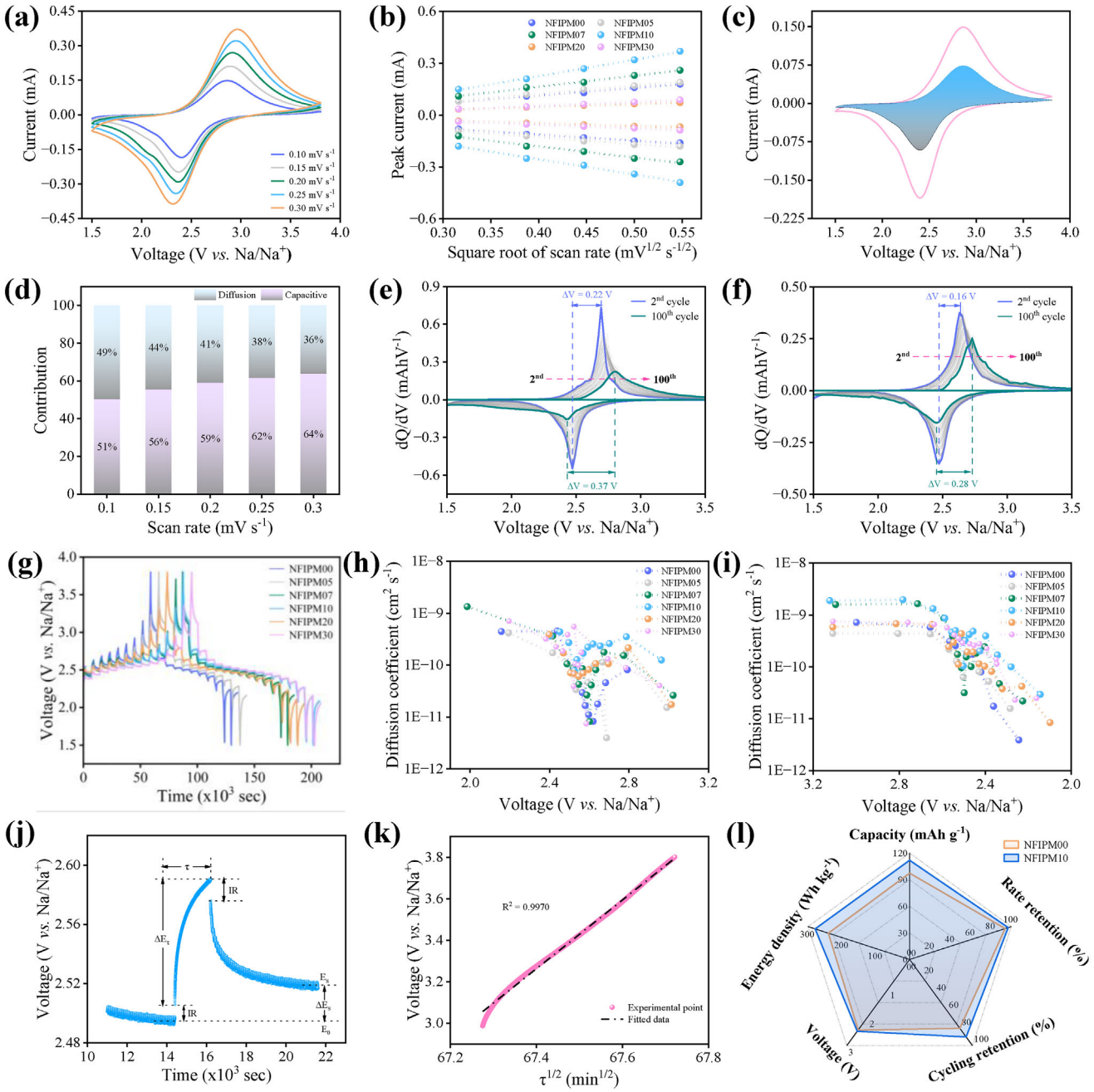


**Figure 5.** a) CV profiles at different scan rates from 0.1 to 0.3 mV $s^{-1}$ for NFIPM10. b) Plot of peak current ($i_p$) versus square root of scan rate ($v^{1/2}$) for all NFIPM electrodes. c,d) Dunn plot at a scan rate of 0.10 mV $s^{-1}$ and percentage capacitive and diffusion contribution for NFIPM10 respectively. Differential capacity plot (dQ/dV) from 2nd to 100th cycles recorded at 0.1C for e) NFIPM00 and f) NFIPM10. g) Galvanostatic intermittent titration technique (GITT) profiles and corresponding charge h) and discharge i) Diffusion coefficients for all cathodes. j) Single titration step and k) Straight line behavior of V versus $\tau^{1/2}$ for NFIPM10. l) Radar plot compares the electrochemical performance of NFIPM00 and optimized NFIPM10.

$Fe^{2+}/Fe^{3+}$ redox couple. In the second cycle, the peak separations were measured as 0.22, 0.16, 0.14, 0.18, 0.10, and 0.32 V for NFIPM00, NFIPM05, NFIPM07, NFIPM10, NFIPM20, and NFIPM30 respectively. Similarly, in the 100$^{th}$ cycle, the peak separations were 0.37, 0.28, 0.20, 0.28, 0.15, and 0.55 V for the same samples. These results indicate that, even after 100 cycles, the $In^{3+}$-doped samples (apart from NFIPM30) exhibit lower cell polarization compared to the undoped sample. Furthermore, after the 100th cycle, NFIPM00 shows a sharp decrease in peak intensity, indicating a reduced specific capacity due to increased cell polarization.

The results of the Rietveld refinement for NFIPM cathodes indicate that $In^{3+}$ doping increases the lattice parameters. The increased unit cell volume due to $In^{3+}$ substitution enhances the

electrochemical performance of the cathode due to improved $Na^+$ mobility. Therefore, the galvanostatic intermittent titration technique (GITT) was employed to determine the $Na^+$ diffusion coefficient of all NFIPM cathodes. The recorded GITT profiles for all NFIPM cathodes in the voltage range of 1.5–3.8 V versus $Na/Na^+$ are shown in Figure 5g. The simplified form of Ficks 2nd law of diffusion can be used to evaluate the $Na^+$ diffusion coefficient as follows:[27]

$$D = \frac{4}{\Pi\tau}\left(\frac{m_B V_m}{M_B\, s}\right)^2\left(\frac{\Delta E_s}{\Delta E_\tau}\right)^2 \left(\tau \ll L^2/D\right) \quad (5)$$

where $V_m$ represents the volume of electrode material (in $cm^3\ mol^{-1}$), $M_B$ defines the molar weight (in $g\ mol^{-1}$), $\tau$ is the applied current pulse time (in sec), $m_B$ stands the mass of cathode (in grams), s is the electrode/electrolyte interfacial contact area (in $cm^2$); $\Delta E_s$ (in V), and $\Delta E_\tau$ (in V) were obtained from each step of titration. To perform the GITT test the values of C-rate, pulse time ($\tau$), and relaxation period were used as 0.1C, 30 min, and 90 min respectively. The charge and discharge $Na^+$ diffusion coefficients for all NFIPM samples are presented in Figure 5h,i respectively. During the discharging process, NFIPM00 exhibits $D_{Na+}$ values ranging from $10^{-10}$ to $10^{-12}\ cm^2\ s^{-1}$, while NFIPM10 shows values between $10^{-9}$ and $10^{-11}\ cm^2\ s^{-1}$. Similarly, during charging, NFIPM00 demonstrates a $D_{Na+}$ range consistent with discharging, whereas NFIPM10 displays values from $10^{-10}$ to $10^{-11}\ cm^2\ s^{-1}$. Notably, NFIPM10 offers higher $D_{Na+}$ values compared to NFIPM00 in both charge and discharge processes. Additionally, the charge/discharge curves reveal a sharp cusp ≈2.5 V, where the lowest $D_{Na+}$ values are observed. This can be attributed to the delayed $Na^+$ intercalation/deintercalation process. These characteristics are typical of electrode materials where flat plateaus are observed in the charge/discharge process.[28] Additionally, the single titration step for NFIPM10 during the charging process is shown in Figure 5j. $\Delta E_\tau$ represents the potential difference between the $E_0$ (initial voltage) and the steady-state potential of $E_s$. Figure 5k represents the linear behavior of voltage versus the square root of $\tau$ validating the assumptions made in deriving the sodium-ion diffusion equation. Further, the disparities in $D_{Na+}$ values obtained from the CV, GITT, and EIS are not uncommon.[28] Specifically, the $D_{Na+}$ values obtained from CV measurements may be low due to the higher concentration gradient observed during the tests. However, NFIPM10 exhibits a higher $Na^+$ diffusion coefficient compared to NFIPM00 obtained from CV, EIS, and GITT. As a result, these measurements highlight that the $In^{3+}$-substitution strategy significantly mitigates kinetic hindrances, thereby improving the electrochemical performance of NFIPM cathodes (Figure 5l).

To further investigate the detailed $Na^+$ reaction kinetics in NFIPM electrodes, electrochemical impedance spectroscopy (EIS) was used. The recorded EIS spectra (in the frequency range of 10 mHz–100 kHz, amplitude of 10 mV) for all NFIPM cathodes show a similar Nyquist plot (**Figure 6a**) consisting of a semicircle at higher to intermediate frequency region and a spike in the lower frequency domain. In general, a 45° spike in the low-frequency region of a Nyquist plot signifies purely diffusion-limited charge transport. However, Figure 6a reveals a combination of pseudocapacitive and diffusion-limited behavior in the cathode material as the angle of the spike does not reflect a perfect Warburg diffusion. Further, the depressed semicircle is composed of surface film and charge transfer resistance while the spike is associated with Warburg impedance. The equivalent circuit model used to fit the EIS spectra is shown in the inset of Figure S18a (Supporting Information). The component of the circuit consists of $R_{[ct+sf]}$, $R_s$, CPE, and $Z_w$ which are attributed to the surface and charge transfer resistance, electrolyte resistance, double layer capacitance, and Warburg impedance respectively. The values of $R_{ct}$ and $R_s$ determined using the electrochemical circuit for NFIPM cathodes are presented in Figure 6b and Table S9 (Supporting Information). The charge transfer resistance ($R_{ct}$) values for NFIPM00, NFIPM05, NFIPM07, NFIPM10, NFIPM20, and NFIPM30 are 370.74, 319.02, 232.17, 185.62, 367.57, and 273.20 Ω, respectively. Notably, all indium-doped samples exhibit lower charge transfer resistance compared to NFIPM00. However, $R_s$ does not show significant changes following $In^{3+}$-substitution, which is expected. The $Na^+$ diffusion coefficient is determined using the EIS data obtained in lower frequency regions based on the following equation:[29]

$$D_{Na+} = \frac{R^2T^2}{2A^2n^4F^4C^2\sigma^2} \quad (6)$$

$$Z_{re} = R_s + R_{ct} + \sigma\omega^{-1/2} \quad (7)$$

where R is the gas constant, T indicates the absolute temperature, A is the surface area of cathode material, n is the number of electrons involved in the electrochemical reaction, F stands for the Faraday constant, C is the bulk concentration of $Na^+$ in electrode, $\sigma$ is the Warburg factor. The plot of $Z_{re}$ versus $\omega^{-1/2}$ is presented in Figure 6c. Notably, the optimized NFIPM10 achieved a $D_{Na+}$ value of $1.32 \times 10^{-9}\ cm^2\ s^{-1}$, which is higher than that of NFIPM00 ($0.40 \times 10^{-11}\ cm^2\ s^{-1}$). To further explore the impact of $In^{3+}$ on the $Na^+$ activation process, EIS was conducted at different temperatures. The EIS spectra for NFIPM10 were recorded after all cells were charged at 2.5 V (Figure 6d) and at 3.8 V versus $Na/Na^+$ (Figure S19b, Supporting Information) following the completion of the first cycle. The apparent activation energy ($E_a$) of $Na^+$ was determined using Butler–Volmer and Arrhenius equations as follows[4]:

$$i_0 = \left(\frac{RT}{nF}\right)\frac{1}{R_{ct}} \quad (8)$$

$$i_0 = A\exp\left(-\frac{Ea}{RT}\right) \quad (9)$$

$$lni_0 = lnA - \frac{Ea}{R}\frac{1}{T} \quad (10)$$

where A represents the temperature-independent coefficient, R depicts the gas constant, T (K) is the absolute temperature, n is the number of electrons participating in the reaction, and F is the Faraday constant. The plot of log ($i_o$) versus (1/T) is displayed in Figure 6e. The activation energy (Ea) can be determined by analyzing the slope of this Figure 6e. NFIPM10 exhibits a lower $E_a$ value ($10.72\ kJ\ mol^{-1}$) at 3.8 V compared to 2.5 V ($17.08\ kJ\ mol^{-1}$).

Moreover, a detailed in-situ EIS study was conducted (in the voltage range of 1.5–3.8 V) to investigate the electrode kinetics

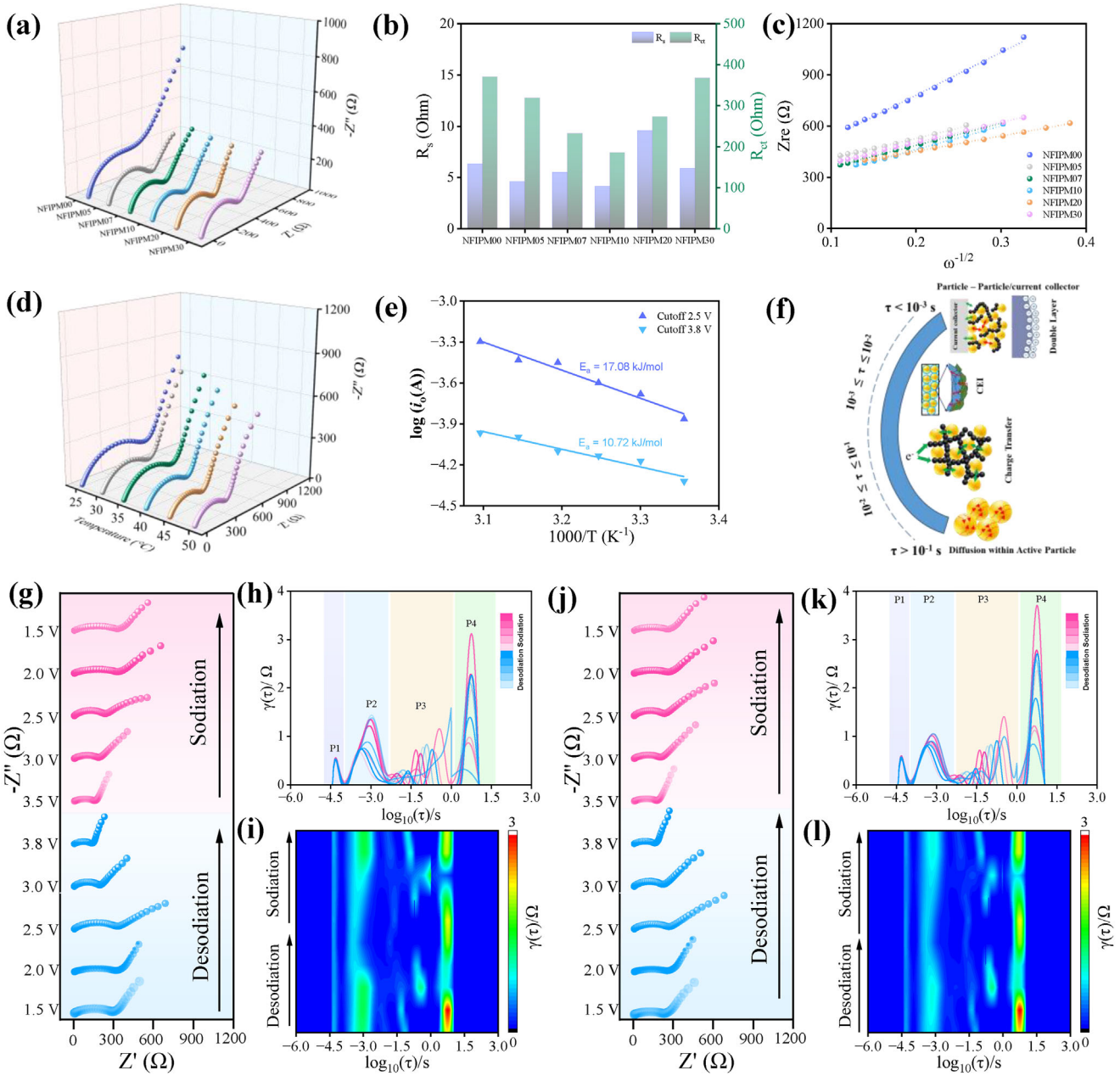


**Figure 6.** Nyquist plots a) and corresponding $R_{ct}$ and $R_s$ b) values were obtained using an equivalent circuit model for all NFIPM cathodes. c) The plot of $Z_{re}$ versus $\omega^{-1/2}$ was obtained from the lower frequency data of the Nyquist plot. d) Temperature-varied EIS plots of NFIPM10 sample recorded at the cell voltage of 2.5 V. e) Arrhenius plots of NFIPM10 cathode. f) Distribution of relaxation times of NFIPM00 and NFIPM10. g) The in situ EIS profiles, h) DRT curves, and i) 2D DRT intensity variation graphs of the NFIPM00. j) The in situ EIS profiles, k) DRT curves, and l) 2D DRT intensity variation graphs of the NFIPM10 during the charge/discharge process.

and interfacial resistance in the NFIPM00 and NFIPM10 cathodes. The analysis was performed on cells after completing the first charge/discharge cycle. The Nyquist plots obtained are displayed in Figure 6g,j, with the fitted EIS spectra and corresponding electrochemical circuit illustrated in Figure S19d (Supporting Information). During desodiation, the surface film resistance ($R_{sf}$) initially increased from 35 to 45.38 Ω for NFIPM00 (Figure S19a, Supporting Information) and from 37 to 42.38 Ω for NFIPM10 (Figure S19c, Supporting Information) within the voltage range of 1.5–2.5 V. This increase in resistance is attributed to the formation of an interfacial film on the electrode surface. The average $R_{sf}$ values observed during desodiation were 34.92 Ω for NFIPM00 and 35.41 Ω for NFIPM10, while the values for the sodiation process were 32.59 and 34.63 Ω, respectively. Overall, both materials exhibited only a slight variation in their $R_{sf}$ values. The lower $R_{sf}$ during the sodiation process indicates reduced electrode/electrolyte interfacial film.[30] Conversely, the higher average charge transfer resistance ($R_{ct}$) of NFIPM00 (173.79 Ω)

compared to NFIPM10 (148.52 Ω) during the entire cycle suggests that a higher transport barrier for $Na^+$ exists in the undoped material.

To further delineate the specific electrochemical processes, we analyzed the EIS data using a distribution of relaxation time (DRT).[31] This mathematical transformation allows us to convert the Nyquist plot from the frequency domain into DRT spectra in the time domain. In details, values of $\tau \leq 10^{-3}$ s correspond to resistance from particle-to-particle and particle-to-current collector (Figure 6f). Values between $10^{-3}$ and $10^{-2}$ s indicate charge transport across the surface film layer. Meanwhile, values ranging from $10^{-2}$ to $10^{-1}$ s reflect charge transport resistance at the electrode interface, and $\tau \geq 10^{-1}$ s represents the resistance associated with bulk electrode diffusion.[32] The four distinct peaks labeled as $P_1$, $P_2$, $P_3$, and $P_4$ are obtained for both NFIPM00 and NFIPM10 cathode during the desodiation/sodiation process (Figure 6h,k). The $P_1$ peaks, located ≈13.3 ms, show significant overlap, indicating the contact resistance measured in the high-frequency domain of the semicircle. The $P_2$ and $P_3$ peaks, with time constants ranging from ≈33.2 to ≈52.30 ms and ≈120.5 to ≈641.97 ms, respectively, for both NFIPM00 and NFIPM10, represent the resistance at the electrode-electrolyte interfaces, as seen in the mid-frequency semicircle. Lastly, the P4 peaks, which ranges from 1.8 to 2.1 s, indicate the bulk electrode diffusion observed in the low-frequency region. The lower relaxation time of 1.80 ms for NFIPM10, compared to 1.88 ms for NFIPM00, indicates reduced impedance for $Na^+$ diffusion in the indium-doped material. The changes in peak intensities during the charge/discharge process are clearly illustrated in the contour plot (Figure 6i,l). In the 2D contour plot for NFIPM10, the $P_2$ peaks shift toward higher relaxation times during the desodiation process (in the voltage range of 1.5–2.5 V). This shift is attributed to the formation of a surface film on the electrode and ion transport through it.[33] On the other hand, during the sodiation process, the $P_2$ peaks shift to the left, indicating an unstable film formation on the electrode. A similar trend was observed for the NFIPM00 cathode.

To gain a more comprehensive understanding of the structural evolution of NFIPM10 during different charge/discharge stages, in-situ XRD analysis was performed for the 1st and 2nd cycle (within a voltage of 1.5–3.8 V) over the $2\theta$ range of 10–50° (**Figure** 7a). At the start of the analysis, several distinct peaks corresponding to the (112), (321), and (420) planes were identified and marked. All marked diffraction peaks reversibly changed throughout the subsequent charge/discharge processes, indicating that NFIPM10 exhibits the single-phase solid-solution reaction and retains structural integrity following electrochemical activation. As the discharge progressed to 2.4 V in the 1st cycle, all Bragg peaks shifted to lower angles, suggesting an expansion in lattice volume due to the gradual insertion of $Na^+$ in the cathode. At the end of the charging process, these peaks returned close to their original positions, reflecting the minimal changes in the structural volume. This behavior was also observed in the 2nd discharge/charge cycle. Moreover, the indexed (420) peak showed a larger $2\theta$ shift (Figure 7b), likely due to the continuous extraction of $Na^+$ increasing the electrostatic interactions between neighboring $Fe^{3+}$ cations and expanding the $FeO_6$ octahedral distance. This increased spacing between octahedra can facilitate $Na^+$ diffusion without impacting the voltage plateau.

The in situ XRD patterns collected during the first cycle were refined using Fullprof to analyze the variation in cell parameters across different electrochemical states. Figure S20 (Supporting Information) displays the refined XRD patterns at the second stage of the discharge process. Figure 7c–e highlights the reversible changes in all three cell parameters corresponding to the observed peaks. Additionally, the electrode exhibited a minimal volume change of ≈8.78% (Figure 7f) reflecting the greater flexibility of the lattice structure during $Na^+$ insertion and extraction. Such minor cell parameter variation and reversible structural evolution significantly contribute to the extended cycling stability of NFIPM10.

Density functional theory (DFT) calculations were conducted to elucidate the impact of dopant on electronic structure, charge distribution, and $Na^+$ migration in both NFIPM00 and NFIPM10 samples. The optimized crystal structures of both samples are shown in Figure S20b,c (Supporting Information). A close agreement between our simulations and experimental data for the values of three lattice parameters was observed, demonstrating the accuracy of the model used to depict NFIPM samples. We then calculated the charge density distribution for both samples (Figure 7g,h) to understand the effect of $In^{3+}$ doping on charge distribution. A uniform charge distribution was observed for the samples irrespective of doping which indicates that $In^{3+}$ substitution helps to retain the structure, ensuring resistance to excess oxidation and ion dissolution during high-current rates over an extended cycling life. A Bader charge analysis.[34] further reveals that charge is uniformly distributed on both the samples, i.e., NFIPM00 (Figure 7j) and NFIPM10 (Figure 7k), indicating the negligible differences in charge depletion or accumulation upon $In^{3+}$ doping in NFIPM samples. Furthermore, electrochemical analysis showed that the charge storage behavior of the electrode material is influenced by a combination of pseudocapacitive and diffusion characteristics. Therefore, climbing-image nudged elastic band (CI-NEB) calculations were performed to investigate the activation barrier for $Na^+$ diffusion in NFIPM00 and NFIPM10. The diffusion pathway and corresponding energy barrier are shown in Figure 7i,k respectively. The NFIPM10 exhibits a lower energy barrier compared to NFIPM00. Thus, $In^{3+}$ substitution enhances the $Na^+$ diffusivity, as experimentally demonstrated in NFIPM10 samples. The density of states (DOS) analysis (Figure 7m,n) reveals that the electron distribution in both the valence and conduction bands of NFIPM10 is more extensive and closer to the Fermi level, indicating enhanced redox reactivity of Fe. Moreover, NFIPM10 shows a reduced bandgap of 0.23 eV compared to 0.44 eV for NFIPM00, confirming that the dopant enhances electrical conductivity. In all, the combined results from DFT calculations and experimental findings strongly highlight the enhanced electrochemical performance of NFIPM10 as compared to the pristine sample, which is attributed to improved electrical conductivity, faster $Na^+$ kinetics, and reduced energy barriers achieved through the selective optimization of $In^{3+}$-doping at the Fe site in NFIPM cathodes.

## 3. Conclusion

In summary, $NaFe_{2-x}In_x(PO_4)(MoO_4)_2$ was successfully synthesized via a solid-state method. Detailed characterization of doped NFIPM showed enhancement in the spin-state post $In^{3+}$

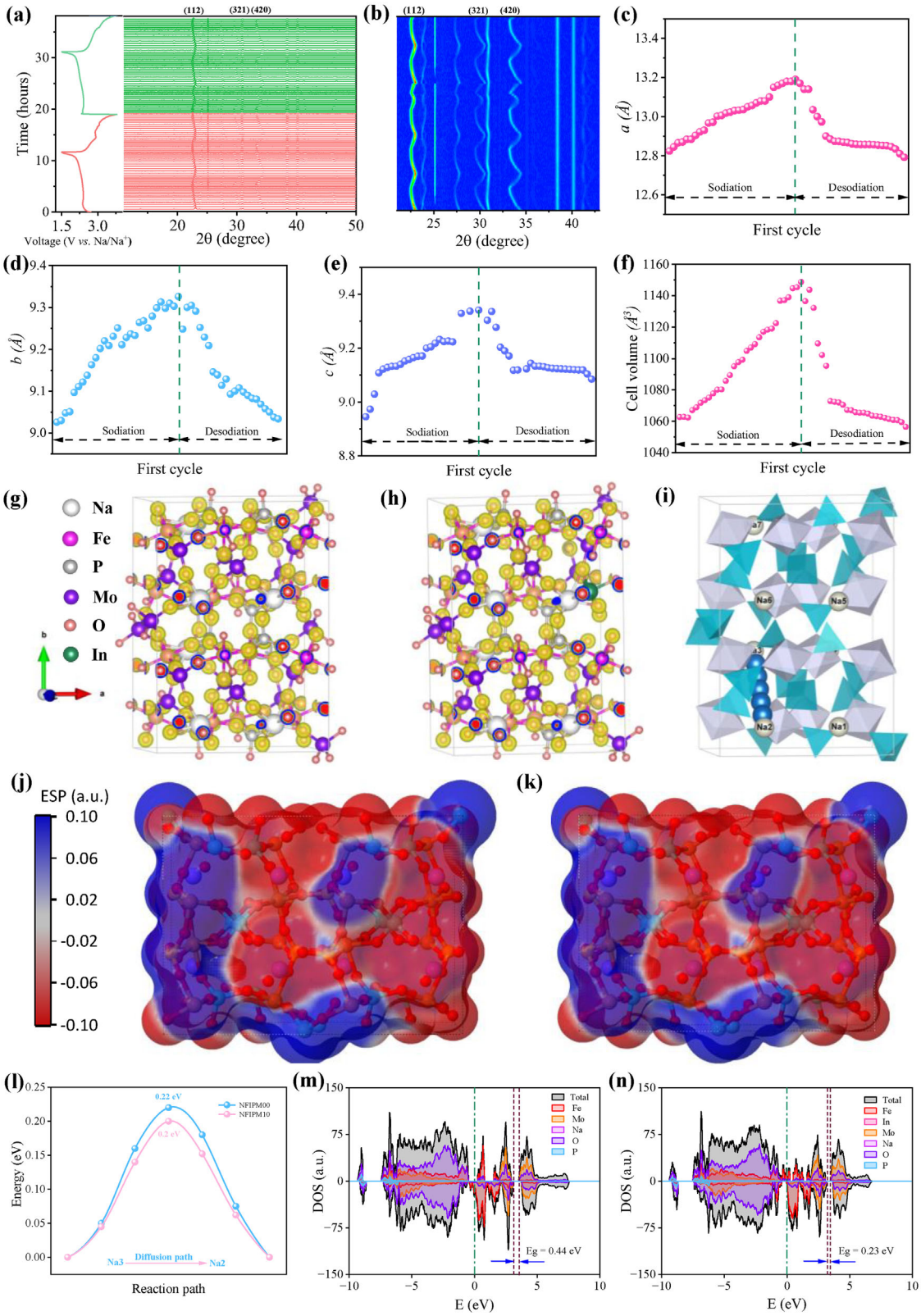


**Figure 7.** a) In situ XRD patterns and corresponding charge-discharge profiles, b) 2D contour plot of the NFIPM10 electrode during 1st and 2nd discharge/charge (in 1.5–3.8 V) process. c–f) Lattice parameter variation at different cell voltages. Charge density distribution of g) NFIPM00 and h) NFIPM10 and Bader charge analysis of j) NFIPM00 and k) NFIPM10. Sodium-ion migration path i), Energy migration barrier l) for NFIPM00 and NFIPM10. Partial density of states (PDOS) and total density of states (TDOS) of m) NFIPM00 and n) NFIPM10.

introduction which helped in reducing the electron-transport resistance in the sample. DFT calculations reveal a lowered bandgap for the $In^{3+}$-substituted NFIPM sample which corroborates with electrical conductivity measurements where the resistance was lowered post-doping. Further, the increased lattice parameters of NFIPM promoted better sodium-ion kinetics, which was also confirmed via the diffusion coefficients obtained through CV, EIS, and GITT. With 0.10 moles of $In^{3+}$ doping, the NFIPM samples were optimized to host sodium ions with a specific capacity of 111.85 mAh $g^{-1}$ with reduced voltage hysteresis. This cathode showed superior structural stability and reversible charge storage up to 600 cycles with ≈75% capacity retention. Nearly 100% coulombic efficiency with an energy density of 280 Wh $kg^{-1}$ was achieved. In situ, XRD revealed a single-phase solid-solution reaction with negligible volume changes during one charge and discharge cycle. We believe that $NaFe_{2-x}In_x(PO_4)(MoO_4)_2$ could inspire the engineering of high-rate, high-voltage, and stable cathodes making such polyanion compounds a competitive candidate to accelerate the industrial adoption of NIBs.

## 4. Experimental Section

*Synthesis of $NaFe_{2-x}In_x(PO_4)(MoO_4)_2$*: Analytical-grade sodium dihydrogen phosphate [$NaH_2PO_4{\cdot}H_2O$, Sigma Aldrich, ≥ 98%], iron nitrate [$Fe(NO_3)_3{\cdot}9H_2O$, Sigma Aldrich, ≥ 98%], indium acetate [$In(C_2H_3O_2)_3$, Sigma Aldrich, ≥ 98%], ammonium molybdate [$(NH_4)_6Mo_7O_{24}{\cdot}4H_2O$, Sigma Aldrich, ≥ 98%], and citric acid [$C_6H_8O_7{\cdot}H_2O$, Sigma Aldrich, ≥ 98%] were used to synthesize $NaFe_{2-x}In_x(PO_4)(MoO_4)_2$ powders (where x = 0.0, 0.05, 0.07, 0.10, 0.20, and 0.30 moles). As an example, for the synthesis of $NaFe_{1.9}In_{0.1}(PO_4)(MoO_4)_2$ (x = 0.10), 1 mmol of $NaH_2PO_4{\cdot}H_2O$, 1.9 mmol of $Fe(NO_3)_3{\cdot}9H_2O$, and 0.1 mmol of $In(C_2H_3O_2)_3$ were added in 100 mL of deionized water at room temperature. This mixture was stirred vigorously at 400 rpm for 30 min, followed by heating at 50 °C for an additional 20 min. Then, 0.29 mmol of $(NH_4)_6Mo_7O_{24}{\cdot}4H_2O$ and 3 mmol of $C_6H_8O_7{\cdot}H_2O$ were added, and the mixture was dried at 120 °C overnight. The powder retrieved was carefully ground and made into pellets and placed in a muffle furnace at 600 °C for 24 h (with a ramp rate of 5 °C $min^{-1}$) to yield $NaFe_{1.9}In_{0.1}(PO_4)(MoO_4)_2$ as the final product. Similar protocols were followed for all $NaFe_{2-x}In_x(PO_4)(MoO_4)_2$ compositions which were labeled as NFIPM00, NFIPM05, NFIPM07, NFIPM10, NFIPM20, and NFIPM30 for x = 0, 0.05, 0.07, 0.10, 0.20, and 0.30 moles, respectively.

*Material Characterizations*: The powder X-ray diffraction (PXRD) was conducted using a PANalytical Empyrean diffractometer with Cu-K$\alpha$ radiation ($\lambda$ = 1.54 Å) over a 2$\theta$ range of 10° to 80°. All diffraction peaks from the powder samples were analyzed through Rietveld refinement using the Foolproof software. The crystal structure of NFIPM cathodes was visualized using VESTA. Thermogravimetric analysis (TGA) was performed via a PERKIN ELMER TGA-8000 instrument. Surface area and pore size distribution were measured via Brunauer–Emmett–Teller (BET) and Barret–Joyner–Halenda (BJH) methods, utilizing $N_2$ adsorption/desorption experiments (using Nova 600 BET, Anton Paar). Electrical conductivity measurements were carried out using a two-point probe method. The temperature-dependent magnetic properties were investigated using Quantum Design PMMS/PMMS-3 magnetometer in the temperature range of 10 K ≤ T ≤ 300 K and magnetic field (H) up to 90 kOe. Low-temperature electron paramagnetic resonance (EPR) experiments were performed by EMX MICRO X, Bruker instrument. Surface functionality and elemental valence states were analyzed using Fourier transform infrared spectroscopy (FTIR, Shimadzu, DRS – 800 A), Raman spectroscopy (Enwave Optronics, USA), and X-ray photoelectron spectroscopy (XPS, Kratos Axis Supra with monochromated Al K$\alpha$ X-ray source). Additionally, scanning electron microscopy (SEM, JEOL, JSM-7610F) and high-resolution transmission electron microscopy (HRTEM, JEOL 2100, 200 kV) with selected area electron diffraction were employed to examine elemental composition, surface features, and morphologies.

*DFT Study*: DFT simulations of the NFIPM00 and NFIPM10 structures were carried out using the Vienna Ab Initio Simulation Package (VASP).[35] The initial structure of NFIPM00 was taken from the Cambridge Crystallographic Data Centre.[1d] A 1 × 2 × 1 supercell consisting of 16 Mo atoms, 16 Fe atoms, 8 P atoms, 8 Na atoms, and 96 O atoms were used for all the calculations. Further, the structure of NFIPM10 was prepared by substituting one of Fe atoms with Indium at random in NFIPM00 representing the structure close to that of $NaFe_{1.9}In_{0.1}(PO_4)(MoO_4)_2$. The optimized structure of NFIPM00 and NFIPM10 was obtained by performing structural minimization by allowing the ionic positions, as well as the size and shape of the simulation box, to change using the Perdew–Burke–Ernzerhof (PBE) function modified for solid materials with the projector augmented wave (PAW) method. An energy cutoff of 520 eV for the plane-wave basis was employed for the optimization calculations. The electronic and ionic relaxation convergence criteria were set to $10^{-6}$ eV and 0.01 Ev $Å^{-1}$, respectively. A climbing image nudged elastic band method,[36] with a spring constant of 5 eV $Å^{-2}$ between the images was employed for finding minimum energy paths and associated energy barriers for $Na^+$ diffusion. Na ion migration between two adjacent sites was assumed, and five intermediate possible structures have been generated between the initial and final configurations of NFIPM00 and NFIPM10. Selective dynamics without allowing the ionic positions of non-migrating atoms, size, and shape of the simulation box to change were performed.

*Electrochemical Characterization*: To perform the electrochemical test of the NFIPM cathode, the electrode material was prepared using a mixture of 80 wt.% active material, 10 wt.% multi-wall carbon nanotubes (MWCNT), and 10 wt.% polyvinylidene (PVDF) binder. To this mixture, N-methyl-2-pyrrolidinone (NMP) was added dropwise and ground with a mortar and pestle to achieve a uniform suspension. The resulting electrode paste was then evenly cast on aluminum foil using a manual doctor blade method and vacuum-dried at 100 °C overnight. Finally, NFIPM electrodes were punched into circular discs with a diameter of 12 mm and stored in an inert atmosphere. Electrochemical tests of $NaFe_{2-x}In_x(PO_4)(MoO_4)_2$ (x = 0.0–0.30) compositions were carried out using CR 2032-coin cells at room temperature. A unit of 1M $NaClO_4$ (Sigma Aldrich, ≥ 98%) solubilized in PC (Sigma Aldrich, ≥ 99%) with 10% (v/v) with additive FEC (Sigma Aldrich, ≥ 99%), glass fiber (GF/C, Whatman), and pure Na-metal (Sigma Aldrich) were used as the electrolyte, separator, and counter electrode respectively. The coin cells were fabricated in a high-purity argon-filled glove box ($H_2O$ ≤ 0.1 ppm, $O_2$ ≤ 0.1 ppm) and rested for 12 h before testing to ensure full electrolyte penetration into the electrode. Galvanostatic charge/discharge (GCD, Neware Battery Tester), cyclic voltammetry (CV, Metrohm AutoLab), and galvanostatic intermittent titration technique (GITT, Metrohm AutoLab) measurements were performed in the voltage range of 1.5–3.8 V versus $Na/Na^+$. Electrochemical impedance spectroscopy (EIS, Metrohm AutoLab) measurements (frequency range = 100 kHz–10 mHz, amplitude = 10 mV) were carried out after the first discharge-charge cycle. The DRT (Distribution of Relaxation Time) analysis was used to interpret the EIS data using an open-source MATLAB GUI-based program (DRT tools).

## Supporting Information

Supporting Information is available from the Wiley Online Library or from the author.

## Acknowledgements

Sharad Pinjari acknowledges IISER-Bhopal for providing fellowship for his PhD. Rohit Ranganathan Gaddam acknowledges the Department of Science and Technology and Anusandhan National Research Foundation (earlier DST-SERB), Government of India for the Startup-Research

Grant (SRG), SRG/2022/001017 and the DST-FIST program, SR/FST/ET-II/2022/1017 (C) for funding the work. The Central Instrumentation Facility of IISER-Bhopal is acknowledged for providing access to material characterization facilities. AKN acknowledges financial support from the Australian Research Council under the ARC Research Hub for Safe and Reliable Energy (IH200100035).

Open access publishing facilitated by University of Southern Queensland, as part of the Wiley - University of Southern Queensland agreement via the Council of Australian University Librarians.

## Conflict of Interest

The author declares no conflict of interest.

## Data Availability Statement

The data that support the findings of this study are available in the supplementary material of this article.

## Keywords

cathode, cell-polarisation, energy density, NASICON, sodium-ion batteries

Received: January 24, 2025
Revised: March 8, 2025
Published online: March 18, 2025

[1] a) S. Guo, Q. Li, P. Liu, M. Chen, H. Zhou, *Nat. Commun.* **2017**, *8*, 135; b) S. W. Kim, D. H. Seo, X. Ma, G. Ceder, K. Kang, *Adv. Energy Mater.* **2012**, *2*, 710; c) H. Pan, Y.-S. Hu, L. Chen, *Energy Environ. Sci.* **2013**, *6*, 2338; d) Y. Wu, Z. Cao, L. Song, J. Gao, *ACS Appl. Mater. Interfaces.* **2021**, *13*, 48865.

[2] a) M. Chen, W. Hua, J. Xiao, D. Cortie, W. Chen, E. Wang, Z. Hu, Q. Gu, X. Wang, S. Indris, *Nat. Commun.* **2019**, *10*, 1480; b) Y. Fang, Z. Chen, L. Xiao, X. Ai, Y. Cao, H. Yang, *Small.* **2018**, *14*, 1703116.

[3] a) B. Ouyang, J. Wang, T. He, C. J. Bartel, H. Huo, Y. Wang, V. Lacivita, H. Kim, G. Ceder, *Nat. Commun.* **2021**, *12*, 5752; b) S. D. Shraer, N. D. Luchinin, I. A. Trussov, D. A. Aksyonov, A. V. Morozov, S. V. Ryazantsev, A. R. Iarchuk, P. A. Morozova, V. A. Nikitina, K. J. Stevenson, *Nat. Commun.* **2022**, *13*, 4097.

[4] Y. Liu, J. Li, Q. Shen, J. Zhang, P. He, X. Qu, Y. Liu, *EScience.* **2022**, *2*, 10.

[5] a) Z. Deng, T. P. Mishra, E. Mahayoni, Q. Ma, A. J. K. Tieu, O. Guillon, J.-N. Chotard, V. Seznec, A. K. Cheetham, C. Masquelier, *Nat. Commun.* **2022**, *13*, 4470; b) S. D. Pinjari, R. C. Dutta, S. Chen, P. Mudavath, X. Huang, J. Bell, S. K. Bhatia, A. K. Nanjundan, R. R. Gaddam, *Chem. Eng. J.* **2024**, *493*, 152485.

[6] K. Shiva, P. Singh, W. Zhou, J. B. Goodenough, *Energy Environ. Sci.* **2016**, *9*, 3103.

[7] a) R. Essehli, A. Alkhateeb, A. Mahmoud, F. Boschini, H. B. Yahia, R. Amin, I. Belharouak, *J. Power Sources.* **2020**, *469*, 228417; b) S.-F. Li, Z.-Y. Gu, J.-Z. Guo, X.-K. Hou, X. Yang, B. Zhao, X.-L. Wu, *J. Mater. Sci. Technol.* **2021**, *78*, 176.

[8] H. Kim, I. Park, S. Lee, H. Kim, K.-Y. Park, Y.-U. Park, H. Kim, J. Kim, H.-D. Lim, W.-S. Yoon, *Chem. Mater.* **2013**, *25*, 3614.

[9] X. Ge, L. He, C. Guan, X. Wang, J. Li, Y. Lai, Z. Zhang, *ACS Nano.* **2023**, *18*, 1714.

[10] a) O. Amin, S. Sinha, P. S. Maji, R. Mukherjee, *J. Solid State Electrochem.* **2023**, *27*, 2387; b) R. Kumar, H. Liu, S. A. Nabavi, M. S. Anyebe, S. Mahesh, H. Snaith, M. Bag, S. M. Jain, *ACS Appl. Electron. Mater.* **2024**, *6*, 8360; c) A. Kumar, P. Bashiri, B. P. Mandal, K. S. Dhindsa, K. Bazzi, A. Dixit, M. Nazri, Z. Zhou, V. K. Garg, A. C. Oliveira, *Inorganics.* **2017**, *5*, 67; d) M. Voccia, S. Kapse, R. Sayago-Carro, N. Gómez-Cerezo, M. Fernández-García, A. Kubacka, F. Viñes, F. Illas, *ACS Appl. Mater. Interfaces.* **2024**, *16*, 30157.

[11] W. Lin, P. Yang, K. Zhou, L. Wang, C. Shen, *Solid State Ionics.* **2023**, *403*, 116322.

[12] a) J. Z. Guo, H. X. Zhang, Z. Y. Gu, M. Du, H. Y. Lü, X. X. Zhao, J. L. Yang, W. H. Li, S. Kang, W. Zou, *Adv. Funct. Mater.* **2022**, *32*, 2209482; b) X. Wang, H. Li, W. Zhang, X. Ge, L. He, L. Zhang, S. Li, N. Wen, J. Guo, Y. Lai, *J. Mater. Chem. A.* **2023**, *11*, 6978; c) Y. Li, Y. Mei, Y. Huang, X. Zhong, Z. Geng, Z. He, H. Ding, W. Deng, G. Zou, T. Liu, *ACS Nano.* **2024**, *18*, 25053;

[13] M. Amanulla, C. M. Magdalane, G. Ramalingam, R. Sundaram, N. Tamam, H. Somaily, M. Al-Buriahi, *Appl. Phys. A.* **2022**, *128*, 397.

[14] a) J. V Barbosa Moura, A. A Gomes de Souza, P. de Tarso Cavalcante Freire, C. da Luz Lima, T. M Brito, F. Oliveira, *Int. J. Appl. Ceram. Technol.* **2021**, *18*, 615; b) T. Ravindran, V. Sivasubramanian, A. K. Arora, *J. Phys.: Condens. Matter.* **2004**, *17*, 277.

[15] Y. Zhou, G. Xu, J. Lin, Y. Zhang, G. Fang, J. Zhou, X. Cao, S. Liang, *Adv. Mater.* **2023**, *35*, 2304428.

[16] Y. Xi, X. Wang, H. Wang, M. Wang, G. Wang, J. Peng, N. Hou, X. Huang, Y. Cao, Z. Yang, *Adv. Funct. Mater.* **2024**, *34*, 2309701.

[17] a) S. Liu, B. Zhang, Y. Cao, H. Wang, Y. Zhang, S. Zhang, Y. Li, H. Gong, S. Liu, Z. Yang, *ACS Energy Lett.* **2022**, *8*, 159; b) J. Li, M. T. Sougrati, A. Zitolo, J. M. Ablett, I. C. Oğuz, T. Mineva, I. Matanovic, P. Atanassov, Y. Huang, I. Zenyuk, *Nat. Catal.* **2021**, *4*, 10.

[18] a) P. Singh, K. Shiva, H. Celio, J. B. Goodenough, *Energy Environ. Sci.* **2015**, *8*, 3000; b) S. D. Pinjari, R. C. Dutta, S. Parshanaboina, P. Mudavath, S. Singha, D. Dubal, X. Wang, J. Bell, A. K. Nanjundan, R. R. Gaddam, *Chem. Eng. J.* **2024**, 157979.

[19] S. D. Pinjari, R. C. Dutta, S. Parshanaboina, P. Mudavath, S. Singha, D. Dubal, X. Wang, J. Bell, A. K. Nanjundan, R. R. Gaddam, *Chem. Eng. J.* **2024**, *502*, 157979.

[20] X. Li, Y. Huang, J. Wang, L. Miao, Y. Li, Y. Liu, Y. Qiu, C. Fang, J. Han, Y. Huang, *J. Mater. Chem. A.* **2018**, *6*, 1390.

[21] M. Li, C. Sun, Q. Ni, Z. Sun, Y. Liu, Y. Li, L. Li, H. Jin, Y. Zhao, *Adv. Energy Mater.* **2023**, *13*, 2203971.

[22] Y. Li, Y. Mei, Y. Huang, X. Zhong, Z. Geng, Z. He, H. Ding, W. Deng, G. Zou, T. Liu, *ACS Nano.* **2024**, *18*, 25053.

[23] P. Li, N. Hu, J. Wang, S. Wang, W. Deng, *Nanomaterials.* **2022**, *12*, 3529.

[24] Y. Liu, C. Sun, Q. Ni, Z. Sun, M. Li, S. Ma, H. Jin, Y. Zhao, *Energy Storage Mater.* **2022**, *53*, 881.

[25] X. Liu, L. Tang, Z. Li, J. Zhang, Q. Xu, H. Liu, Y. Wang, Y. Xia, Y. Cao, X. Ai, *J. Mater. Chem. A.* **2019**, *7*, 18940.

[26] J. Zhang, X. Zhao, Y. Song, Q. Li, Y. Liu, J. Chen, X. Xing, *Energy Storage Mater.* **2019**, *23*, 25.

[27] C. J. Wen, B. Boukamp, R. A. Huggins, W. Weppner, *J. Electrochem. Soc.* **1979**, *126*, 2258.

[28] Y. Hou, Q. Liu, L. Yang, J. Hu, Z. Wang, X. Zhang, J. Pan, Z. Bai, H. Wang, Z. Lu, *Small.* **2023**, *19*, 2207466.

[29] H. Liu, C. Li, H. Zhang, L. Fu, Y. Wu, H. Wu, *J. Power Sources.* **2006**, *159*, 717.

[30] C. Sun, Y. Zhao, Q. Ni, Z. Sun, X. Yuan, J. Li, H. Jin, *Energy Storage Mater.* **2022**, *49*, 291.

[31] T. H. Wan, M. Saccoccio, C. Chen, F. Ciucci, *Electrochim. Acta.* **2015**, *184*, 483.

[32] a) X. Zhou, J. Huang, Z. Pan, M. Ouyang, *J. Power Sources.* **2019**, *426*, 216; b) X. Chen, L. Li, M. Liu, T. Huang, A. Yu, *J. Power Sources.* **2021**, *496*, 229867; c) J. Pati, R. S. Dhaka, *J. Power Sources.* **2024**, *609*, 234646.

 

[33] a) T. Ji, X. Liu, T. Zhang, Y. Shi, D. Sheng, H. Yin, Z. X. Shen, D. Chao, *Adv. Energy Mater.* **2024**, *14*, 2401908; b) Z. Chen, X. Wu, Z. Sun, J. Pan, J. Han, Y. Wang, H. Liu, Y. Shen, J. Li, D. L. Peng, *Adv. Energy Mater.* **2024**, *14*, 2400132.

[34] a) G. Henkelman, A. Arnaldsson, H. Jónsson, *Comput. Mater. Sci.* **2006**, *36*, 354; b) W. Tang, E. Sanville, G. Henkelman, *J. Phys.: Condens. Matter.* **2009**, *21*, 084204.

[35] a) G. Kresse, J. Hafner, *Phys. Rev. B.* **1993**, *47*, 558; b) G. Kresse, J. Furthmüller, *Phys. Rev. B.* **1996**, *54*, 11169; c) G. Kresse, J. Furthmüller, *Comput. Mater. Sci.* **1996**, *6*, 15.

[36] a) D. Sheppard, P. Xiao, W. Chemelewski, D. D. Johnson, G. Henkelman, *J. Chem. Phys.* **2012**, *136*, 074103; b) D. Sheppard, G. Henkelman, *J. Comput. Chem.* **2011**, *32*, 1769; c) D. Sheppard, R. Terrell, G. Henkelman, *J. Chem. Phys.* **2008**, *128*, 134106.